Templating Effects in Molecular Growth of Blended Films for Efficient Small–Molecule Photovoltaics

4 AUTHORS, INCLUDING:

Zhiping Wang
National Institute of Advanced Industrial Scie…
10 PUBLICATIONS **59** CITATIONS

SEE PROFILE

Toshihiro Yamanari
Chemical Materials Evaluation and Research B…
42 PUBLICATIONS **717** CITATIONS

SEE PROFILE

Yuji Yoshida
National Institute of Advanced Industrial Scie…
**121** PUBLICATIONS **1,845** CITATIONS

SEE PROFILE

Templating Effects in Molecular Growth of Blended Films for Efficient Small-Molecule Photovoltaics

Zhiping Wang,*,[†] Tetsuhiko Miyadera,*,[†,‡] Toshihiro Yamanari,[†] and Yuji Yoshida[†]

[†]Research Center for Photovoltaic Technologies, National Institute of Advanced Industrial Science and Technology (AIST), AIST Tsukuba Central 5, 1-1-1, 305-8568 Higashi, Tsukuba, Japan

[‡]JST-PRESTO, Japan Science and Technology Agency (JST), 4-1-8 Honcho, 332-0012 Kawaguchi, Saitama, Japan

S *Supporting Information*
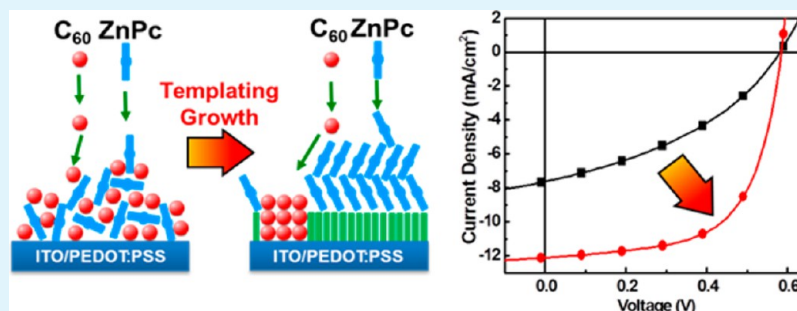
ABSTRACT: A strategy to control the molecular growth of coevaporated zinc phthalocyanine (ZnPc) and fullerene (C_{60}) blended films for efficient organic photovoltaic (OPV) cells was demonstrated. Introduction of a 2,5-bis(4-biphenylyl)-bithiophene (BP2T) film or a ZnPc film on BP2T as nanostructured templates not only results in phase-separated domains in blended films with clear interpenetrating networks but also improves the crystallinity of ZnPc domains, both of which enhance photocurrent generation and charge carrier transport. Such morphology is strongly associated with the molecular growth of the templating layers. Roughness and adhesion of the templating layers are of great importance for the molecular growth of the blended films and in turn for cell characteristics. By carefully regulating the molecular growth of the blended films, the power conversion efficiency was improved by 125%, from 1.85 to 4.15% under 1 sun.

KEYWORDS: *templating effects, molecular growth, organic blended film, organic photovoltaics*

■ INTRODUCTION

Organic photovoltaic (OPV) cells are considered to be promising candidates for future photovoltaic applications owing to their flexibility in usage and low production cost.[1,2] For a long time, the power conversion efficiency (PCE) of OPV cells has been limited by Frankel excitons with short diffusion length.[3] One of the major breakthroughs in cell PCE was achieved by the introduction of a bulk heterojunction (BHJ) architecture consisting of a blend of donor and acceptor molecules.[4−6] The highest PCE reported to date for a single heterojunction reached 9.2% in a polymer-based BHJ cell[7] and 8.9% in a small-molecule BHJ cell.[8] The widely dispersed donor−acceptor (D−A) interface in a BHJ improves exciton separation and allows the use of thicker absorption layers, thus harvesting more sunlight.[9] However, the random molecular growth of donor and acceptor materials in blended films can lead to a high recombination rate due to the poorly defined pathways for charge extraction. Methods for growing ordered blended films with phase-separated morphologies that guarantee interconnected networks for photogenerated holes and electrons toward the electrodes are crucial for overcoming this challenge.[10,11]

For solution-processed OPV cells, thermal or solvent annealing of the blended layer are generally used as means of obtaining phase-separated morphologies.[12,13] In the case of vacuum-processed OPV cells featuring small-molecules, most of the donors and acceptors displayed comparable sizes in blended films, which makes it difficult to form phase-separated morphologies. Extensive efforts have been made to optimize the blended films by improving molecular growth during the coevaporation, such as heating treatments,[14−16] alternative deposition,[17] changing the mixing ratio of donor and acceptor,[18] and introducing buffer layers.[19]

Templating growth is one of the most effective methods in controlling the molecular growth of organic films.[20−25] Recent studies[26,27] suggest that templating growths are effective in morphological modification of donor materials for efficient OPV cells. Copper iodide (CuI) templates grown on indium tin oxide (ITO) by glancing angle deposition enables lying-down growth of zinc phthalocyanine (ZnPc) with nanopillar geometry, which significantly improves light absorption and

simultaneously enlarges the D−A interface for exciton dissociation in ZnPc/fullerene (C_{60}) bilayer cells.[26] Crystalline diindenoperylene films can act as structural templates for the molecular growth of tetraphenyldibenzoperiflanthene (DBP), which not only led to a much larger D−A interface over a conventional planar film but also profoundly promote the exciton transfer in DBP films.[27] However, most of the templating effects are merely inspected in pure films for planar-type OPVs. Discussions on templating effects in blended films for BHJ-type OPVs remain scarce. Previous studies demonstrated that introduction of CuI or 2,5-bis(4-biphenyl-yl)-bithiophene (BP2T) as a template layer improved the crystalline growth of ZnPc in the coevaporation process, which greatly enhanced performances of BHJ-type OPVs.[28,29] Yet, it remains challenging in precise control/optimization of the templating growth of the blended films because of the lack of understanding the templating effects in molecular growth. Here, we investigate the templating effects in coevaporated ZnPc:C_{60} blended films via governing the molecular growths of BP2T (Figure S1, Supporting Information (SI)) and ZnPc as nanostructured templates. Introduction of BP2T or ZnPc on BP2T templates enables a phase-separated morphology in ZnPc:C_{60} blended films. This morphology can be further controlled by regulating the molecular growth of the templating layers. Cells with an optimized morphology showed a high power conversion efficiency of 4.15% under 1 sun.

■ EXPERIMENTAL SECTION

A 40 nm layer of poly(3,4-ethylenedioxythiophene):poly-(styrenesulfonate) (PEDOT:PSS) was spin-coated on indium tin oxide (ITO) and annealed at 135 °C on a hot plate for 30 min under ambient atmosphere. Prior to use, BP2T (Aldrich) and ZnPc (Aldrich) were purified three times by vacuum gradient sublimation, whereas C_{60} (Frontier Carbon, 99.9%) and bathocuproine (BCP; Dojindo, 98%) were used as received. Devices were fabricated with the typical i−n architecture ITO/PEDOT:PSS/template layer (BP2T: 5 nm)/i-layer (ZnPc:C_{60} blend: 40 nm)/n-layer (C_{60}: 20 nm)/ BCP (3 nm)/Al (100 nm) (Figure 4a) and with typical p−i−n architecture by inserting the p-layer (ZnPc: 5, 10, and 20 nm) between BP2T and the i-layer (Figure 9a). All materials were thermally evaporated onto the substrates in a vacuum chamber (<5 × 10^{-6} Pa) at different substrate temperatures: room temperature (RT) for the BP2T, 150 °C for the p-layer, 90 °C for the i-layer, and RT for the remaining layers. The deposition rates were set at 0.5, 0.1, 0.1, 0.3, and 1 Å/s for BP2T, ZnPc, C_{60}, BCP, and Al, respectively. The BHJ i-layers were fabricated by the coevaporation of ZnPc and C_{60} films at a blending ratio of 1:1. For reference, an OPV cell was fabricated with an i−n architecture using the same process as that used for growing the i-layer but without the BP2T templating layer. The active device area was 4 mm². At least eight devices were prepared to obtain the standard deviations. The current density−voltage (J−V) characteristics of the cells were measured under simulated solar illumination (AM 1.5G) using a digital source meter (Keithley 2400). The incident power was calibrated using a standard silicon photovoltaic to match 1 sun intensity (100 mW/cm²). External quantum efficiency (EQE) spectra were collected using a xenon lamp that was integrated with a computer-controlled monochromator, and the source power spectrum was measured using a calibrated silicon photodiode. To calculate the internal quantum efficiency (IQE), the absolute reflectance of an actual cell was measured with an

integrating sphere system. Crystal structures were characterized by X-ray diffraction (XRD) analysis using the Bragg−Brentano configuration with a 9 kW rotating anode generator (Rigaku). The surface morphology was observed using atomic force microscopy (AFM; Nanonavi/E-sweep, SII nanotechnology) in contact mode.

■ RESULTS AND DISCUSSION

First of all, the initial growth characteristics of coevaporated ZnPc:C_{60} films on ITO/PEDOT:PSS (without BP2T, SI Figure S2a) and ITO/PEDOT:PSS/BP2T (with BP2T, SI Figure S2b) were investigated by AFM, as shown in Figure 1.
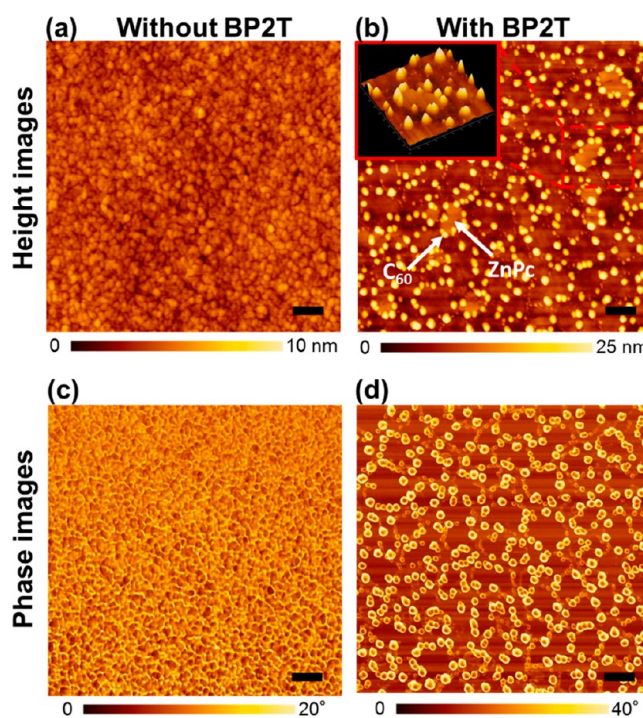

Figure 1. AFM height images of (a) a 2 nm blended film on ITO/ PEDOT:PSS; (b) a 2 nm blended film on ITO/PEDOT:PSS/BP2T (inset: enlarged 3D image); the corresponding AFM phase images are in (c) and (d). The scale bars are 100 nm in all cases.

Figure 1a,c show, respectively, height- and phase-contrast images of a 2 nm blended film without BP2T. Small round grains were observed, and a phase separation structure could not be identified in either the height or phase images. Figure 1b,d show, respectively, height- and phase-contrast images of a 2 nm blended film on BP2T. The corresponding, enlarged 3D image is shown in the inset of Figure 1b. The coevaporated molecules clearly exhibited two totally different growth patterns: flat crystallites on BP2T domains and small round grains at BP2T domain boundaries. Because phase images are sensitive to variations in material properties,[30] the large phase contrast between the flat crystallites and small round grains in Figure 1d indicate that two distinct materials were grown on the BP2T domains and at the domain boundaries. To identify these two materials, pure ZnPc and C_{60} films were deposited on BP2T, as shown in Figure 2a,b, respectively. Pure ZnPc and C_{60} films showed very different growth patterns on BP2T templates. ZnPc molecules grew preferentially on BP2T domains and reflected the BP2T domain shape (Figure 2a). Moreover, the ZnPc domains were observed to be textured/
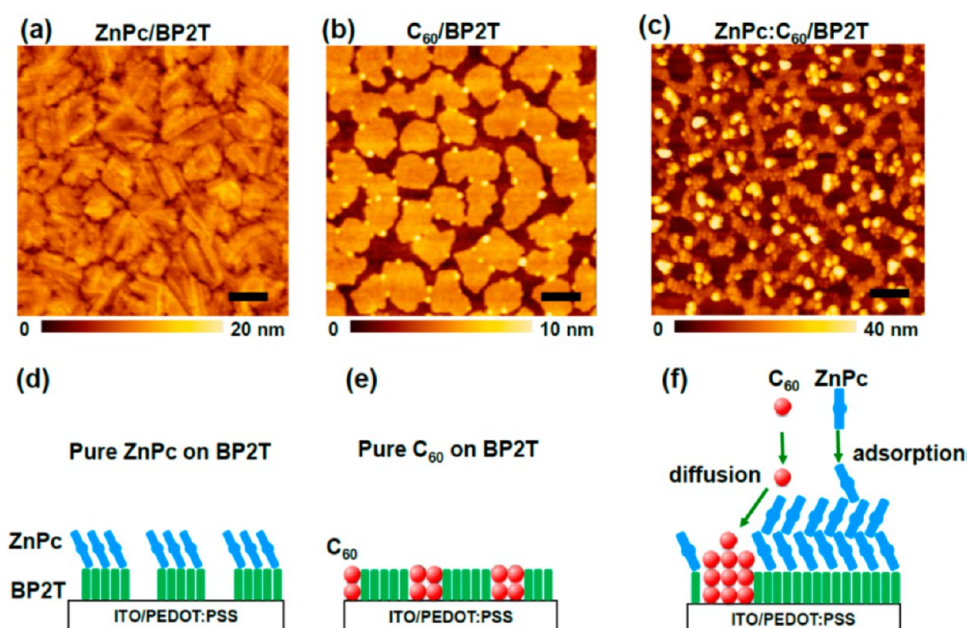
Figure 2. AFM height images of (a) a 5 nm ZnPc film on BP2T (b) a 1 nm C_{60} film on BP2T, and (c) a 10 nm blended film on BP2T. The scale bars are 100 nm in all cases. The corresponding growth modes of (a)−(c) are schematically illustrated in (d)−(f), respectively.
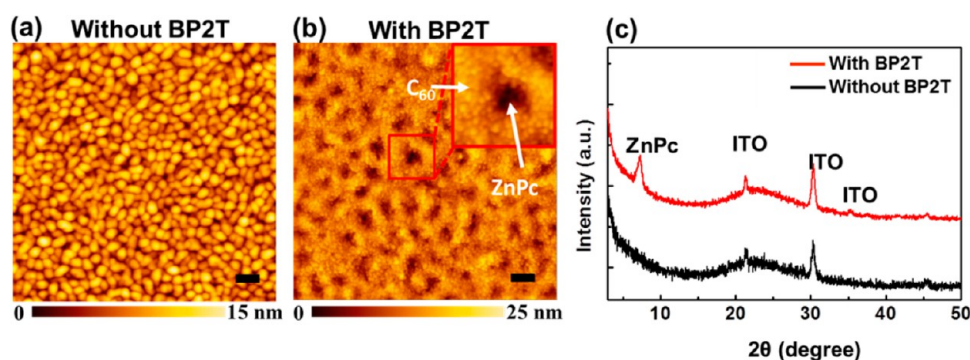

Figure 3. AFM height images of a 40 nm blended film on (a) ITO/PEDOT:PSS (without BP2T) and (b) ITO/PEDOT:PSS/BP2T (with BP2T); inset is an enlarged domain image. The scale bars are 100 nm in all cases. (c) The corresponding XRD patterns. The diffraction peaks at $2\theta = 21.5$, 30.5, and 35.4° are due to the ITO substrate (polycrystalline In_2O_3).

oriented on BP2T, indicating an excellent crystallinity. It seems that the large BP2T crystalline plates provided a clean surface (SI Figure S2b,d) for ZnPc growth. On the other hand, C_{60} molecules were observed to grow at domain boundaries rather than on the domain surface (Figure 2b). A very similar phenomenon was also observed in the growth of pure C_{60} on crystallized ZnPc film (SI Figure S3). It is inferred that C_{60} prefers to grow on the defects at domain boundaries in initial growth. Therefore, in the blended film (Figure 1b), the materials on the BP2T domains and at the boundaries were identified as ZnPc and C_{60}, respectively.

Generally, the molecule−substrate interfacial interaction and intermolecular interaction dominate the film growth. Zhou et al. reported that utilizing the template distributed with strong interaction areas and weak interaction areas enables the phase separation in the coevaporation process.[28] However, in our case, the effect of the templating layer is quite different. It has been reported that BP2T molecules prefer to stand upright on an amorphous ITO/PEDOT:PSS substrate,[31,32] and therefore, only weak van der Waals interactions rather than strong $\pi−\pi$ stacking interaction exists between the BP2T template and the

coevaporated molecules. In this sense, instead of interfacial interaction, the surface diffusion process is more likely to dominate the initial growth of the blended film. It has been proved that molecular diffusion can play a significant role in molecular assembly, and the diffusion (dynamics) of molecules depends on the molecular 3D shape and the atomic registry of the substrate.[33] We believe that the diffusivity of molecules with an anisotropic disk shape, like ZnPc, should be lower as compared with molecules with an isotropic football shape, like C_{60}. On the clean surface of the BP2T domains, the spherical C_{60} molecules are easier to diffuse freely to occupy the sites with minimum surface energy at the domain boundaries (defects), whereas the ZnPc molecules are easier to crystallize on the domain surface. Therefore, a phase-separated morphology (Figure 1b) was observed in the initial growth of the blended film on BP2T. In a 10 nm blended film on BP2T (Figure 2c), the coevaporated ZnPc and C_{60} molecules continue to rearrange so as to keep away from each other. The initially deposited ZnPc and C_{60} molecules can serve as precursors (seed layer) for the lateral growth of the coevaporated molecules (Figure 2f). Moreover, the C_{60}
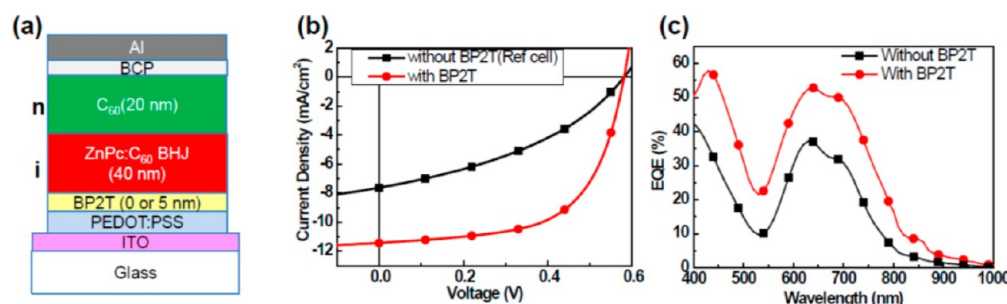
Figure 4. (a) Schematic structure of the i−n structured OPV cells, (b) *J*−*V* characteristics, and (c) the corresponding EQE spectra.

Table 1. Summary of Device Parameters for i−n-Structured OPV Cells with and without BP2T Templating Layer[a]

cells	PCE (%)	J_{sc} (mA/cm^2)	V_{oc} (V)	FF
without BP2T (ref cell)	1.85 ± 0.24	7.58 ± 0.08	0.58	0.42 ± 0.05
with BP2T	3.93 ± 0.08	11.68 ± 0.04	0.58	0.58 ± 0.01

[a]The reference cell structure is i−n architecture on ITO/PEDOT:PSS.

molecules were found to fill all the boundaries forming continuous pathways, which would promote efficient charge carrier transport. Note that domain boundaries are usually considered to be defects during crystal growth of organic films;[34] however, they can serve as C$_{60}$ growth sites in coevaporation to obtain a phase-separated morphology.

Figure 3a,b show, respectively, the morphologies of 40 nm ZnPc:C$_{60}$ blended films with and without BP2T. The XRD patterns of these two blended films are shown in Figure 3c. The blended film without BP2T displayed continuous film morphology with small isolated domains. The corresponding XRD showed that apart from the ITO peaks originated from the substrate, no diffraction peak from the blended film was identified. Without BP2T, the coevaporated ZnPc and C$_{60}$ molecules diffused randomly on the amorphous surface of ITO/PEDOT:PSS and formed nucleation sites on each other, resulting in intermixing domains (Figure 3a). Although the size of these domains was relatively large, no long-range order existed inside these domains, and therefore, no diffraction peak was observed. Comparatively, on BP2T, the blended film displayed a totally different morphology consisting of low separated domains (dark fields) and high interpenetrating domains (bright fields), as shown in Figure 3b. To better understand the morphology, the corresponding 3D image was shown in SI Figure S4. We found that at the same deposition rate, C$_{60}$ grew much higher than ZnPc along vertical direction. Judging from the initial and intermediate growth, it is reasonable to believe that the low fields/domains correspond to ZnPc and the high fields/domains correspond to C$_{60}$ (Figure 3b inset). The corresponding XRD (Figure 3c) showed a diffraction peak at around $2\theta = 7°$, which comes from the standing-up ZnPc diffraction. Combined with the morphological difference (ZnPc domains were textured/oriented on BP2T and had a large mosaicity on PEDOT:PSS), it suggests that the crystallinity of ZnPc domains in the blended film was significantly enhanced by the presence of BP2T. Pure ZnPc films have been demonstrated to exhibit greatly improved crystallinity on BP2T.[29] Our results inferred that ZnPc molecules remained a strong intermolecular interaction (crystal growth) with each other on BP2T domains even during the coevaporation process and simultaneously repelled C$_{60}$ molecules to BP2T domain boundaries, which is consistent with the AFM observation. It has been found that the

introduction of BP2T templating layer not only enables templating growth of the blended films forming a phase-separated morphology with interpenetrating networks but also enhances the crystallinity of the ZnPc domains in the blended films.

To examine the effects of the BP2T templating growth in photovoltaic characteristics, the current−voltage (*J*−*V*) characteristics of i−n structured OPV cells are presented in Figure 4b and Table 1. Compared to the reference cell (without BP2T), devices with BP2T showed remarkable increases in fill factor (FF) from 0.42 to 0.59 and short-circuit current (*J*sc) from 7.58 to 11.46 mA/cm^2, which resulted in a 112% increase in PCE from 1.82 to 3.93%. The wavelength dependence of *J*sc was analyzed by EQE spectra, as shown in Figure 4c. The cells with BP2T exhibited a significant increase in photocurrent generation in both the C$_{60}$ (400−500 nm) and ZnPc (550−850 nm) regions. Overall photovoltaic characteristics have been substantially improved via BP2T templating growth. To clarify the origin of the improvement, IQE is calculated from the ratio of EQE and spectral absorption, as shown in Figure 5. The cell
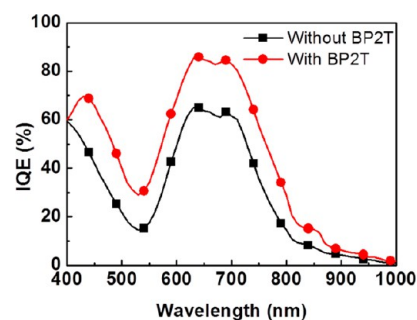

Figure 5. IQE spectra of the i−n structured OPV cells.

with BP2T had a higher IQE over the entire excitation spectrum compared to the cell without BP2T. The increase should be attributed to increased interface area. Note that the maximum efficiency at $\lambda = 430$ and 630 nm was as high as 70 and 86%, respectively. To reach such a high IQE, it is necessary to simultaneously achieve efficient light absorption, exciton diffusion, charge separation, and carrier collection. Physically, this indicates a close to ideal active layer morphology, with an interpenetrating network, which is consistent with AFM
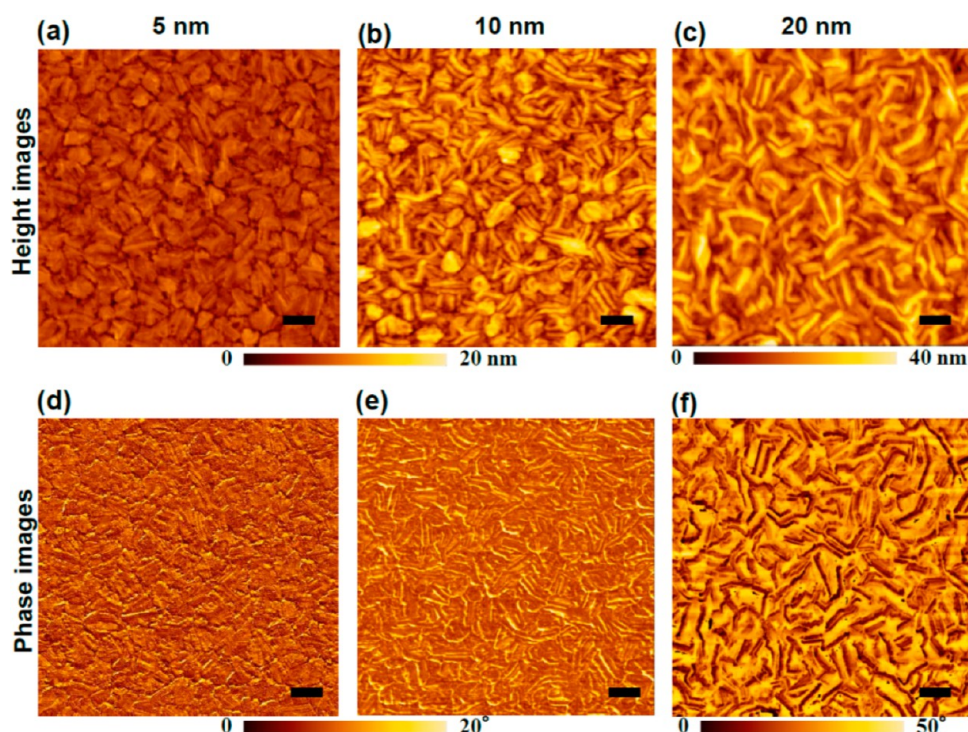
Figure 6. (a)−(c) AFM height images of p-layer films on ITO/PEDOT:PSS/BP2T of varying p-layer thickness: (a) 5, (b) 10, and (c) 20 nm; the corresponding phase images are in (d)−(f), respectively. The scale bars are 100 nm in all cases. The root-mean-square (RMS) roughness values for (a), (b), and (c) are 1.8, 2.5, and 4.6 nm, respectively.
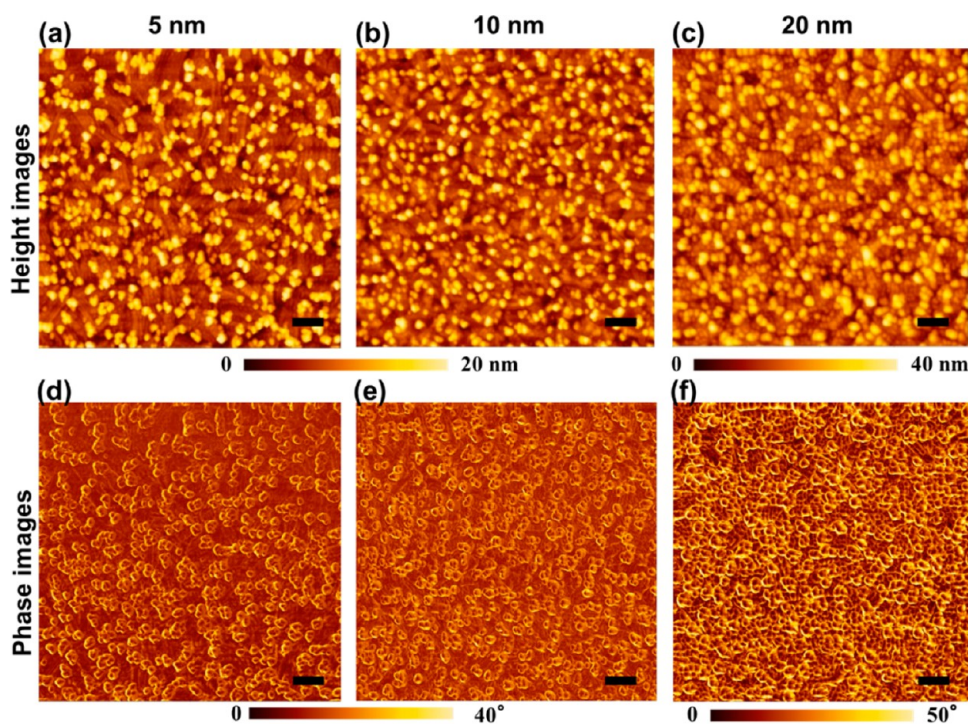

Figure 7. AFM height images of 10 nm blended films on a (a) 5, (b) 10, and (c) 20 nm p-layer; the corresponding phase images are in (d)−(f), respectively. The scale bars are 100 nm in all cases.

observation (Figure 2c). The blended film without BP2T displayed randomly formed, small isolated domains of ZnPc and C_{60} (Figure 3a). These small isolated domains would result in a high density of trap sites inside the blend film, which greatly degrades the charge transport efficiency, owing to recombination.[28] Therefore, the cell without BP2T showed a very poor FF of 0.42. In contrast, the blended film with BP2T templating growth displayed a phase-separated morphology with interpenetrating networks (Figure 3b), as well as the enhanced crystallinity in ZnPc domains (Figure 3c), both of which greatly improved the charge carrier transport,[35−37] resulting in a 40% increase in FF. It is worth pointing out
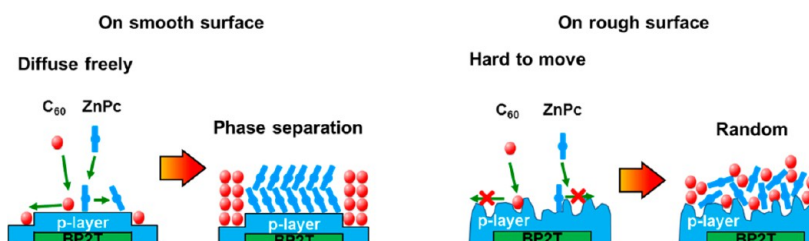
6373

dx.doi.org/10.1021/am405740c | ACS Appl. Mater. Interfaces 2014, 6, 6369−6377

Figure 8. Schematic of growth modes of coevaporated molecules on different p-layers.
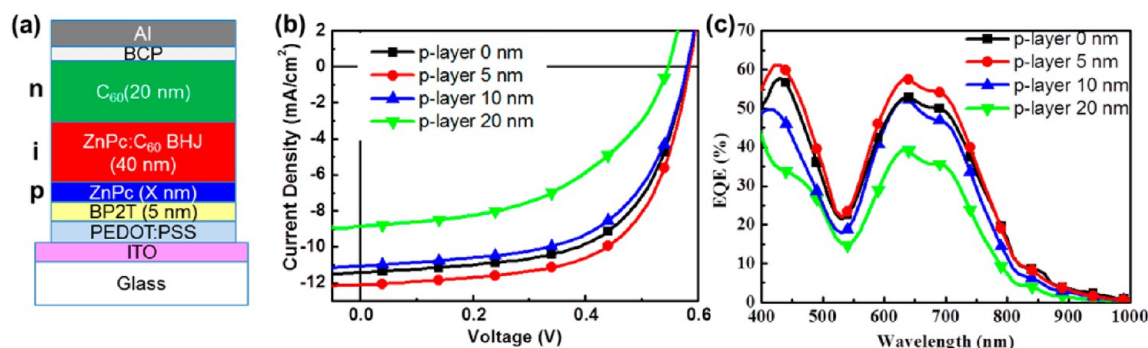

Figure 9. (a) Schematic structure of the p−i−n-structured OPV cells, (b) J−V characteristics, and (c) the corresponding EQE spectra with p-layer 0 nm equal to i−n structure.

that the phase-separated domain size was about 40−100 nm (Figure 3b), which is slightly larger than the typical exciton diffusion length (below 40 nm).[38] This could be a disadvantage for achieving efficient exciton dissociation in spite of a fact that a high J_{sc} was observed. The deficit in the large phase-separated domain size can be compensated by the enhanced crystallinity in ZnPc domains due to the extended exciton diffusion length.[39−41] As a result, a 50% increase in J_{sc} from 7.58 to 11.46 mA/cm^2 was observed. Within the XRD detection limit, there was no improvement in the crystallinity of C_{60} in the BHJ films, despite the enhanced EQE spectra in the C_{60} region. Many authors have reported that an improved donor intermolecular interaction can enhance the crystallinity of both the donor and acceptor materials.[42,43] The crystallinity of the C_{60} domains in the present study was presumably also improved, although this would need to be confirmed by further examination, such as transmission electron microscopy.

Compared with i-n structured OPV cells, p−i−n structure is well-known to further improve cell performance by introducing a pure p-layer under blended films.[44] Here, pure ZnPc films with different thicknesses were inserted between the BP2T and blended films serving as p-layers. The better energy alignment and electron blocking with a pure p-layer has been confirmed to enhance PCE.[45,46] Apart from that, structural and morphological properties of p-layers might also play an important role in molecular growth of blended i-layers and in turn affect cell performances. Figure 6 shows the height- and phase-contrast AFM images of the pure p-layers on BP2T with different p-layer thicknesses. The morphology of a 5 nm p-layer (Figure 6a) reflected the shape of BP2T domains with a very smooth surface (RMS roughness: 1.8 nm). The corresponding phase image (Figure 6d) showed large contrasts between domains and boundaries and small contrast across each domain. When the p-layer thickness was increased to 10 nm (Figure 6b), the p-layer morphology still reflected the domain shape. However, a fiber structure started to emerge on each domain, which was associated with standing-up ZnPc crystallites.[29,34] This fiber

growth not only increased the roughness to 2.5 nm but also resulted in a higher phase contrast (Figure 6e). As the p-layer thickness increased further to 20 nm (Figure 6c), the p-layer no longer retained the domain shape. Instead, the fibers on neighboring domains began to join, resulting in a coarse surface (RMS roughness: 4.6 nm). The corresponding phase image (Figure 6f) exhibited a much higher phase contrast. Many studies suggested that the phase contrast has close connection with the energy dissipation seen in adhesion hysteresis.[47−57] Higher phase contrast (brighter fields), especially at domain boundaries and at facets of ZnPc fibers, indicates larger adhesion force. Both surface roughness and the surface adhesion force were observed to increase with increasing p-layer thickness. The molecule growth of the blended films would be greatly associated with these different p-layer surfaces.

Figure 7 shows the AFM height-contrast and phase-contrast images of the blended films on the different p-layers. The corresponding, enlarged images were also provided in SI Figure S5. The blended film displayed a phase-separated morphology with a clear interpenetrating network on a 5 nm p-layer (Figure 7a,d and SI Figure S5a). Instead of staying on the surface of the ZnPc domains, the C_{60} still diffused to the boundaries, which indicates that only very weak intermolecular interaction exists between the standing ZnPc molecule and the C_{60} molecule. The phase-separated morphology slightly degraded on a 10 nm p-layer (Figure 7b,e and SI Figure S5b). When increasing the p-layer thickness to 20 nm (Figure 7c,f and SI Figure S5c), the blended film displayed a relatively random morphology (almost lost all phase separation and percolation features). From the point of view of the kinetic process, the growth models of blended films on the different p-layers are illustrated in Figure 8. On a smooth surface (thin p-layers), the C_{60} molecules can diffuse with a long mean-free path to the defects at domain boundaries, and the ZnPc molecules are able to crystallize on the clean domain surface. Therefore, the phase-separated morphologies were observed with thin p-layers. In contrast, on a rough surface (thick p-layers), the coevaporated molecules

Table 2. Summary of Device Parameters for p−i−n-Structured OPV Cells with Different P-Layer Thicknesses

cells	PCE (%)	J_{sc} (mA/cm^2)	V_{oc} (V)	FF
p-layer (0 nm)	3.93 ± 0.08	11.68 ± 0.04	0.58	0.58 ± 0.01
p-layer (5 nm)	4.15 ± 0.05	12.34 ± 0.06	0.58	0.58 ± 0.01
p-layer (10 nm)	3.66 ± 0.12	11.07 ± 0.08	0.58	0.57 ± 0.01
p-layer (20 nm)	2.39 ± 0.23	9.03 ± 0.30	0.55	0.48 ± 0.03

have to overcome higher energy barriers which greatly hinders the templating growth, leading to a random morphology. On the other hand, from the view of the surface adhesive properties, the coevaporated molecules have much higher probability to be trapped on an adhesive surface (thick p-layers), leading to a random growth. Consequently, the phase-separated morphology was observed to degrade as the p-layer thickness increases. A smooth and less-adhesive p-layer surface is favorable to the templating growth of a blended film.

The J−V characteristics of p−i−n structured OPV cells are presented in Figure 9b and Table 2. The overall photovoltaic characteristics were highly dependent on the p-layer thickness. Comparing p−i−n with i−n, the slight increase in J_{sc} comes from the photocurrent generation of the 5 nm ZnPc. However, further increasing the p-layer thickness greatly degraded the overall cell performances. The cells exhibited a high FF and J_{sc} at 5 nm, which decreased slightly at 10 nm and dramatically at 20 nm. It has been observed that increasing p-layer thickness led to coarse and adhesive surfaces (Figure 6). These surfaces greatly hindered the templating growth of the blended films, resulting in discontinuous pathways (Figure 7b,c), which is adverse to carrier extraction due to recombination. Therefore, the cells showed a decreasing FF with increasing p-layer thickness. The EQE spectra in Figure 9c suggested that the cell exhibited high efficiencies with a 5 nm p-layer and then decreased in both the C_{60} and ZnPc regions with increasing p-layer thickness. A 5 nm p-layer exhibited a smooth and less-adhesive surface (Figure 6a,d), which allows the coevaporated molecules to diffuse a long distance to grow crystalline domains. The excitons generated in these well-crystallized domains can easily diffuse to the dissociation sites (D−A interfaces), which directly contributes to the photocurrent generation. Thus, the maximum EQE at the C_{60} and ZnPc regions was as high as 58% and 61%, respectively, in the cell with a 5 nm p-layer. The 10 and 20 nm p-layers exhibited a rough and adhesive surface, which would disrupt the crystal growth of both ZnPc and C_{60} domains, resulting in a low exciton dissociation rate. Therefore, the decreased J_{sc} as well as the decreased EQE in both the ZnPc and C_{60} regions were observed. Furthermore, the rough and adhesive surface would also lead to a relatively high density of growth defects (vacancies), resulting in a higher energy loss, which would account for the decrease in open-circuit voltage (V_{oc}) from 0.58 to 0.55 V in the cell with a 20 nm p-layer. The BP2T templating effects in photovoltaic characteristics can be simply concluded as follows: (1) Templating-growth-induced phase-separated morphology with interpenetrating network guarantees the charge carrier transport, resulting in a 40% increase in FF. (2) Enhanced crystallinity of the separated domains enables a higher exciton dissociation rate, resulting in a 50% increase in Jsc. (3) Deposition of a pure ZnPc layer on BP2T not only function as a p-layer for the p−i−n structured cell but also as a structural template for the phase separation in the blended film. Rough and adhesive p-layer surfaces disturb the construction of interpenetrating networks, resulting in the decreased FF, and

simultaneously worsen the domain crystallinity, resulting in the decreased J_{sc}. It is worth mentioning that another reason for the decrease of cell performance could also be the resistivity of the thick ZnPc layer. To clarify this potential influencing factor, p−i−n structured OPV cells without the BP2T templating layer were fabricated, as shown in SI Figure S6. However, no significant decrease in the overall cell performance was observed with increasing p-layer thickness. Consequently, we believe that the decrease in the performances of BP2T-templated p−i−n cell with thick p-layers is mainly associated with the surface characteristics rather than the resistivity of p-layers. A smooth and less-adhesive surface of the p-layers is essential to obtain excellent photovoltaic characteristics.

■ CONCLUSIONS

In summary, we have demonstrated that BP2T or ZnPc on BP2T can function as a nanostructured template capable of inducing phase-separated morphologies in the ZnPc:C_{60} blended films, which significantly improves the cell performances. On BP2T or ZnPc templates, coevaporated ZnPc and C_{60} molecules constantly kept away from each other forming a phase-separated morphology. The templating growth not only realized the construction of interpenetrating networks in the blended films for carrier transport but also enhanced the crystallinity of the ZnPc domains in the blended films for efficient exciton dissociation. Furthermore, such templating-growth-directed morphologies closely associated with the growth characteristics of the templating layers. Rough and adhesive surfaces of the templating p-layer significantly degraded the phase separation in the blended films due to the hindered templating growth, resulting in a decreased J_{sc} and FF. By optimizing the templating growth, the J_{sc} and FF were improved by 60% and 40%, respectively, which resulted in a 125% increase in PCE from 1.85 to 4.15% under 1 sun. Through this systematic study, we find a substantial opportunity for improving the performance of small-molecule photovoltaics by careful control of molecular growth in the blended films, and we highlight the importance of analyzing the templating effects to enable an integrate optimization.

■ ASSOCIATED CONTENT

ⓢ Supporting Information

Additional information includes molecular structure description, energy alignment, and substrate morphology. This material is available free of charge via the Internet at http://pubs.acs.org.

■ AUTHOR INFORMATION

Corresponding Authors
*E-mail: (Z.-P.W.) wang-zhiping@aist.go.jp.
*E-mail: (T.M.) tetsuhiko-miyadera@aist.go.jp.

Notes

The authors declare no competing financial interest.

◼ REFERENCES

(1) Liu, Y. S.; Yang, Y. (Michael); Chen, C.-C.; Chen, Q.; Dou, L. T.; Hong, Z. R.; Li, G.; Yang, Y. Solution-Processed Small Molecules using Different Electron Linkers for High-Performance Solar Cells. *Adv. Mater.* **2013**, *25*, 4657−4662.

(2) Krebs, F. C. Fabrication and Processing of Polymer Solar Cells: A Review of Printing and Coating Techniques. *Sol. Energy Mater. Sol. Cells* **2009**, *93*, 394−412.

(3) McGehee, M. D.; Topinka, M. A. Solar Cells: Pictures from the Blended Zone. *Nat. Mater.* **2006**, *5*, 675−676.

(4) Yu, G.; Gao, J.; Hummelen, J. C.; Wudl, F.; Heeger, A. J. Polymer Photovoltaic Cells: Enhanced Efficiencies via a Network of Internal Donor−Acceptor Heterojunctions. *Science* **1995**, *270*, 1789−1791.

(5) Halls, J. J. M.; Walsh, C. A.; Greenham, N. C.; Marseglia, E. A.; Friend, R. H.; Moratti, S. C.; Holmes, A. B. Efficient Photodiodes from Interpenetrating Polymer Networks. *Nature* **1995**, *376*, 498−500.

(6) Lunt, R. R.; Giebink, N. C.; Belak, A. A.; Benziger, J. B.; Forrest, S. R. Exciton Diffusion Lengths of Organic Semiconductor Thin Films Measured by Spectrally Resolved Photoluminescence Quenching. *J. Appl. Phys.* **2009**, *105*, 053711.

(7) He, Z. C.; Zhong, C. M.; Su, S. J.; Xu, M.; Wu, H. B.; Cao, Y. Enhanced Power-Conversion Efficiency in Polymer Solar Cells Using an Inverted Device Structure. *Nat. Photonics* **2012**, *6*, 593−597.

(8) Kyaw, A. K. K.; Wang, D. H.; Wynands, D.; Zhang, J.; Nguyen, T.-Q.; Bazan, G. C.; Heeger, A. J. Improved Light Harvesting and Improved Efficiency by Insertion of an Optical Spacer (ZnO) in Solution-Processed Small-Molecule Solar Cells. *Nano Lett.* **2013**, *13*, 3796−3801.

(9) Lin, Y. Z.; Lia, Y. F.; Zhan, X. W. Small Molecule Semiconductors for High-Efficiency Organic Photovoltaics. *Chem. Soc. Rev.* **2012**, *41*, 4245−4272.

(10) Peumans, P.; Uchida, S.; Forrest, S. R. Efficient Bulk Heterojunction Photovoltaic Cells Using Small-Molecular-Weight Organic Thin Films. *Nature* **2003**, *425*, 158−162.

(11) Schunemann, C.; Wynands, D.; Wilde, L.; Hein, M. P.; Pfutzner, S.; Elschner, C.; Eichhorn, K. J.; Leo, K.; Riede, M. Phase Separation Analysis of Bulk Heterojunctions in Small-Molecule Organic Solar Cells using Zinc-Phthalocyanine and C_{60}. *Phys. Rev. B* **2012**, *85*, 245314.

(12) Walker, B.; Kim, C.; Nguyen, T. Q. Small Molecule Solution-Processed Bulk Heterojunction Solar Cells. *Chem. Mater.* **2011**, *23*, 470−482.

(13) Facchetti, A. π-Conjugated Polymers for Organic Electronics and Photovoltaic Cell Applications. *Chem. Mater.* **2011**, *23*, 733−758.

(14) Pfuetzner, S.; Meiss, J.; Petrich, A.; Riede, M.; Leo, K. Thick C_{60}:ZnPc Bulk Heterojunction Solar Cells with Improved Performance by Film Deposition on Heated Substrates. *Appl. Phys. Lett.* **2009**, *94*, 253303.

(15) Osasa, T.; Yamamoto, S.; Matsumura, M. Organic Solar Cells by Annealing Stacked Amorphous and Microcrystalline Layers. *Adv. Funct. Mater.* **2007**, *17*, 2937−2942.

(16) Pfuetzner, S.; Mickel, C.; Jankowski, J.; Hein, M.; Meiss, J.; Schuenemann, C.; Elschner, C.; Levin, A. A.; Rellinghaus, B.; Leo, K.; Riede, M. The Influence of Substrate Heating on Morphology and Layer Growth in C_{60}:ZnPc Bulk Heterojunction Solar Cells. *Org. Electron.* **2011**, *12*, 435−441.

(17) Kim, J. W.; Kim, H. J.; Lee, H. H.; Kim, T.; Kim, J. J. Formation of Bulk Heterojunctions by Alternative Thermal Deposition and Its Structure Analysis for High Efficiency Small Molecular Organic Photovoltaics. *Adv. Funct. Mater.* **2011**, *21*, 2067−2071.

(18) Pandey, R.; Holmes, R. J. Graded Donor−Acceptor Heterojunctions for Efficient Organic Photovoltaic Cells. *Adv. Mater.* **2010**, *22*, 5301−5305.

(19) Zeng, W.; Yong, K. S.; Kam, Z. M.; Zhu, F.; Li, Y. Effect of Blend Layer Morphology on Performance of ZnPc:C_{60}-Based Photovoltaic Cells. *Appl. Phys. Lett.* **2010**, *97*, 133304.

(20) Heutz, S.; Cloots, R.; Jones, T. S. Structural Templating Effects in Molecular Heterostructures Grown by Organic Molecular-Beam Deposition. *Appl. Phys. Lett.* **2000**, *77*, 3938−3940.

(21) Derri, M.; Wu, W.; Fleet, L. R.; Harrison, N. M.; Hirjibehedin, C. F.; Kay, C. W. M.; Fisher, A. J.; Aeppli, G.; Heutz, S. High-Temperature Antiferromagnetism in Molecular Semiconductor Thin Films and Nanostructures. *Nat. Commun.* **2014**, *5*, 3079.

(22) Hinderhofer, A.; Hosokai, T.; Frank, C.; Novák, J.; Gerlach, A.; Schreiber, F. Templating Effect for Organic Heterostructure Film Growth: Perfluoropentacene on Diindenoperylene. *J. Phys. Chem. C* **2011**, *115*, 16155−16160.

(23) Hinderhofer, A.; Gerlach, A.; Kowarik, S.; Zontone, F.; Krug, J.; Schreiber, F. Smoothing and Coherent Structure Formation in Organic−Organic Heterostructure Growth. *Europhys. Lett.* **2010**, *91*, 56002.

(24) Barrena, E.; de Oteyza, D. G.; Sellner, S.; Dosch, H.; Osso, J. O.; Struth, B. In Situ Study of the Growth of Nanodots in Organic Heteroepitaxy. *Phys. Rev. Lett.* **2006**, *97*, 076102.

(25) Zhang, Y.; Barrena, E.; Zhang, X.; Turak, A.; Maye, F.; Dosch, H. J. New Insight into the Role of the Interfacial Molecular Structure on Growth and Scaling in Organic Heterostructures. *J. Phys. Chem. C* **2010**, *114*, 13752−13758.

(26) Zhou, Y.; Taima, T.; Miyadera, T.; Yamanari, T.; Kitamura, M.; Nakatsu, K.; Yoshida, Y. Glancing Angle Deposition of Copper Iodide Nanocrystals for Efficient Organic Photovoltaics. *Nano Lett.* **2012**, *12*, 4146−4152.

(27) Zhou, Y.; Taima, T.; Kuwabara, T.; Takahashi, K. Efficient Small-Molecule Photovoltaic Cells using a Crystalline Diindenoperylene Film as a Nanostructured Template. *Adv. Mater.* **2013**, *25*, 6069−6075.

(28) Zhou, Y.; Taima, T.; Miyadera, T.; Yamanari, T.; Kitamura, M.; Nakatsu, K.; Yoshida, Y. Phase Separation of Co-Evaporated ZnPc:C_{60} Blend Film for Highly Efficient Organic Photovoltaics. *Appl. Phys. Lett.* **2012**, *100*, 233302.

(29) Yu, B.; Huang, L.; Wang, H.; Yan, D. Efficient Organic Solar Cells using a High-Quality Crystalline Thin Film as a Donor Layer. *Adv. Mater.* **2010**, *22*, 1017−1020.

(30) Scott, W. W.; Bhushan, B. Use of Phase Imaging in Atomic Force Microscopy for Measurement of Viscoelastic Contrast in Polymer Nanocomposites and Molecularly Thick Lubricant Films. *Ultramicroscopy* **2003**, *97*, 151−169.

(31) Yang, J. L.; Wang, T.; Wang, H. B.; Zhu, F.; Li, G.; Yan, D. H. Ultrathin-Film Growth of para-Sexiphenyl (II): Submonolayer Thin-Film Growth as a Function of the Substrate Temperature. *J. Phys. Chem. B* **2008**, *112*, 7816−7820.

(32) Yang, J. L.; Wang, T.; Wang, H. B.; Zhu, F.; Li, G.; Yan, D. H. Ultrathin-Film Growth of Para-Sexiphenyl (II): Formation of Large-Size Domain and Continuous Thin Film. *J. Phys. Chem. B* **2008**, *112*, 7821−7825.

(33) Otero, R.; Hümmelink, F.; Sato, F.; Legoas, S. B.; Thostrup, P.; Lægsgaard, E.; Stensgaard, I.; Galvão, D. S.; Besenbacher, F. Lock-and-Key Effect in the Surface Diffusion of Large Organic Molecules Probed by STM. *Nat. Mater.* **2004**, *3*, 779−782.

(34) Yang, J. L.; Yan, D. H. Weak Epitaxy Growth of Organic Semiconductor Thin Films. *Chem. Soc. Rev.* **2009**, *38*, 2634−2645.

(35) Karl, N. Charge Carrier Transport in Organic Semiconductors. *Synth. Met.* **2003**, *133−134*, 649−657.

(36) Forrest, S. R.; Kaplan, M. L.; Schmidt, P. H. Organic-on-Inorganic Semiconductor Contact Barrier Diodes. II. Dependence on Organic Film and Metal Contact Properties. *J. Appl. Phys.* **1984**, *56*, 543−551.

(37) Shtein, M.; Mapel, J.; Benziger, J. B.; Forrest, S. R. Effects of Film Morphology and Gate Dielectric Surface Preparation on the Electrical Characteristics of Organic-Vapor-Phase-Deposited Pentacene Thin-Film Transistors. *Appl. Phys. Lett.* **2002**, *81*, 268−270.

(38) Yang, F.; Shtein, M.; Forrest, S. R. Controlled Growth of a Molecular Bulk Heterojunction Photovoltaic Cell. *Nat. Mater.* **2005**, *4*, 37−41.

(39) Lunt, R. R.; Benziger, J. B.; Forrest, S. R. Relationship between Crystalline Order and Exciton Diffusion Length in Molecular Organic Semiconductors. *Adv. Mater.* **2010**, *22*, 1233−1236.

(40) Rim, S. B.; Fink, R. F.; Schoneboom, J. C.; Erk, P.; Peumans, P. Effect of Molecular Packing on the Exciton Diffusion Length in Organic Solar Cells. *Appl. Phys. Lett.* **2007**, *91*, 173504.

(41) Terao, Y.; Sasabe, H.; Adachi, C. Correlation of Hole Mobility, Exciton Diffusion Length, and Solar Cell Characteristics in Phthalocyanine/Fullerene Organic Solar Cells. *Appl. Phys. Lett.* **2007**, *90*, 103515.

(42) Osaka, I.; Saito, M.; Mori, H.; Koganezawa, T.; Takimiya, K. Drastic Change of Molecular Orientation in a Thiazolothiazole Copolymer by Molecular-Weight Control and Blending with PC$_{61}$BM Leads to High Efficiencies in Solar Cells. *Adv. Mater.* **2012**, *24*, 425−430.

(43) Sun, Y.; Welch, G. C.; Leong, W. L.; Takacs, C. J.; Bazan, G. C.; Heeger, A. J. Solution-Processed Small-Molecule Solar Cells with 6.7% Efficiency. *Nat. Mater.* **2012**, *11*, 44−48.

(44) Walzer, K.; Maennig, B.; Pfeiffer, M.; Leo, K. Highly Efficient Organic Devices Based on Electrically Doped Transport Layers. *Chem. Rev.* **2007**, *107*, 1233−1271.

(45) Hiramoto, M.; Fiujiwara, H.; Yokoyama, M. Three-Layered Organic Solar Cell with a Photoactive Interlayer of Codeposited Pigments. *Appl. Phys. Lett.* **1991**, *58*, 1062−1064.

(46) Chen, G.; Sasabe, H.; Wang, Z. Q.; Wang, X. F.; Hong, Z. R.; Yang, Y.; Kido, J. Co-Evaporated Bulk Heterojunction Solar Cells with >6.0% Efficiency. *Adv. Mater.* **2012**, *24*, 2768−2773.

(47) Tamayo, J.; Garcia, R. Deformation, Contact Time, and Phase Contrast in Tapping Mode Scanning Force Microscopy. *Langmuir* **1996**, *12*, 4430−4435.

(48) Tamayo, J.; Garcia, R. Effects of Elastic and Inelastic Interactions on Phase Contrast Images in Tapping-Mode Scanning Force Microscopy. *Appl. Phys. Lett.* **1997**, *71*, 2394−2396.

(49) Garcia, R.; Tamayo, J.; Calleja, M.; Garcia, F. Phase Contrast in Tapping-Mode Scanning Force Microscopy. *Appl. Phys. A: Mater. Sci. Process.* **1998**, *66*, S309−S312.

(50) Gotsmann, B.; Seidel, C.; Anczykowski, B.; Fuchs, H. Conservative and Dissipative Tip-Sample Interaction Forces Probed with Dynamic AFM. *Phys. Rev. B* **1999**, *60*, 11051.

(51) Jourdan, J. S.; Cruchon-Dupeyrat, S. J.; Huan, Y.; Kuo, P. K.; Liu, G. Y. Imaging Nanoscopic Elasticity of Thin Film Materials by Atomic Force Microscopy: Effects of Force Modulation Frequency and Amplitude. *Langmuir* **1999**, *15*, 6495−6504.

(52) Bar, G.; Delineau, L.; Brandsch, R.; Ganter, M.; Whangbo, M.-H. Hysteresis in the Distance-Sweep Curves of Elastomers and Its Implications in Tapping Mode Atomic Force Microscopy. *Surf. Sci.* **2000**, *457*, L404−L412.

(53) Basnar, B.; Friedbacher, G.; Brunner, H.; Vallant, T.; Mayer, U.; Hoffmann, H. Analytical Evaluation of Tapping Mode Atomic Force Microscopy for Chemical Imaging of Surfaces. *Appl. Surf. Sci.* **2001**, *171*, 213−225.

(54) James, P. J.; Antognozzi, M.; Tamayo, J.; McMaster, T. J.; Newton, J. M.; Miles, M. J. Interpretation of Contrast in Tapping Mode AFM and Shear Force Microscopy. A Study of Nafion. *Langmuir* **2000**, *17*, 349−360.

(55) Anczykowski, B.; Gottsman, B.; Fuchs, H.; Cleveland, J. P.; Elings, V. B. How to Measure Energy Dissipation in Dynamic Mode Atomic Force Microscopy. *Appl. Surf. Sci.* **1999**, *140*, 376−382.

(56) Bar, G.; Delineau, L.; Brandsch, R.; Bruch, M. Importance of the Indentation Depth in Tapping-Mode Atomic Force Microscopy Study of Compliant Materials. *Appl. Phys. Lett.* **1999**, *75*, 4198−4200.

(57) Tamayo, J.; Garcia, R. Relationship between Phase Shift and Energy Dissipation in Tapping-Mode Scanning Force Microscopy. *Appl. Phys. Lett.* **1998**, *73*, 2926−2928.

6377

dx.doi.org/10.1021/am405740c | *ACS Appl. Mater. Interfaces* 2014, 6, 6369−6377